energies

MDPI

Article

A Perylenediimide-Based Zinc-Coordination Polymer for Photosensitized Singlet-Oxygen Generation

Simon N. Deger †, Sebastian J. Weishäupl †, Alexander Pöthig * and Roland A. Fischer *

Chair of Inorganic and Metal-Organic Chemistry, Catalysis Research Center, Ernst-Otto-Fischer-Straße 1, 85748 Garching, Germany; simon.deger@tum.de (S.N.D.); sebastian.weishaeupl@tum.de (S.J.W.)
* Correspondence: alexander.poethig@tum.de (A.P.); roland.fischer@tum.de (R.A.F.)
† These authors contributed equally to this work.

Abstract: In the face of anthropogenic global warming the design and synthesis of materials, which enable energy transfer processes using sunlight as an energy source, are of high interest. Perylenediimides are a highly absorbing class of chromophores suitable for sunlight absorption and conversion. Therefore, metal–organic frameworks (MOFs) and coordination polymers (CPs) with incorporated organic perylene chromophores are highly interesting materials both for applied, but also fundamental, photophysical research. MOFs/CPs have the advantage of a modular adjustability of interchromophoric distances and angles, and the choice of metal nodes can be used to further tune the material towards the desired photophysical properties. In the present paper, we present a study using a reported organic perylenediimide (PDI) chromophore (H_2tpdb) as a linker to be incorporated into coordination polymer and test towards applicability within the photochemical $^1O_2$ generation. In detail, a novel zinc 2D -coordination polymer Zn(tpdb)$(DMF)_3$ is reported, which is synthesized using a solvothermal synthesis with $Zn(NO_3)_2$ and a ditopic organic perylene linker. Both the linker and Zn-CP are fully characterized, including SC-XRD, showing a strong aggregation of tightly packed chromophores in the solid state. The photophysical properties are examined and discussed, including the observed shifts within the absorption spectra of the CP are compared to the linker in solution. These shifts are mainly attributed to the for PDIs known H-type aggregation and an additional charge transfer in the framework structure, causing a limited quantum yield of the emission. Finally, the photosensitization of triplet oxygen to singlet oxygen using 1,3-diphenylisobenzofurane (DBPF) as a trapping agent is investigated both for the free linker and the Zn-CP, showing that the perylene chromophore is an efficient photosensitizer and its activity can, in principle, be retained after its incorporation in the coordination polymer.

Keywords: perylene diimide; metal–organic framework; singlet oxygen; photosensitizer; H-type aggregation

Citation: Deger, S.N.; Weishäupl, S.J.; Pöthig, A.; Fischer, R.A. A Perylenediimide-Based Zinc-Coordination Polymer for Photosensitized Singlet-Oxygen Generation. *Energies* **2022**, *15*, 2437. https://doi.org/10.3390/en15072437

Academic Editor: Claudio Mele

Received: 18 February 2022
Accepted: 21 March 2022
Published: 25 March 2022

1. Introduction

In the light of anthropogenic global warming, a conversion of greenhouse gases (e.g., CO_2 and NO_x) into valuable chemicals is the focus of current research [1]. In nature, light-absorbing dyes, such as chlorophyll, are utilized to convert light into energy-rich organic compounds, primarily carbohydrates, from low-energy inorganic substances, such as carbon dioxide and water [2,3].

Therefore, translating the fundamental reactions of natural photosynthesis into an efficient, robust, and economic *artificial leaf* is a significant task [2,4,5]. In order to be able to design and fabricate high-performance synthetic materials, a deep understanding of related energy transfer processes inside these compounds is of utmost importance.

Metal–organic frameworks (MOFs) are a class of porous, polymeric, and multifunctional hybrid materials. They consist of metal ions and organic bridging ligands, and therefore the respective research is located at the interface between molecular coordination

chemistry and materials science [6]. In the presented study, the metal ions serve as nodes of a crystalline lattice. They govern the structure and topology of the material n combination with the directionality of the organic linkers [7].

Additionally, the wide range of possible metal nodes as well as the different design concepts of the organic linker molecules offer a variety of magnetic, electrical, optical, and catalytic properties that can be incorporated into these materials. For instance, MOFs have been applied in catalysis, gas storage, telecommunications, photovoltaics, or sensor technology applications [8–13].

With respect to the photochemical properties of the material, MOF chemistry offers a precise control of pore size and interchromophoric distances and angles, therefore, in principle, providing synthetic tools to fundamentally study energy-transfer processes and the reactivity of the material [9,14].

Concerning the choice of chromophore linkers, rylene dyes are a very prominent class of organic dye molecules. Initially applied for industrial use as red dyes and as pigments in automotive finishes [15], they became widely used in manifold industrial applications as well as in modern research [16], due to their outstanding chemical, thermal, and optical stability [17–19]. In addition, they exhibit remarkable optoelectronic properties, e.g., as excellent light-harvesting materials, since they strongly absorb visible light with high fluorescence quantum yields in solution [20]. Furthermore, they possess a large conjugated π-system, as well as high molar absorption coefficients, which results in strong intermolecular coupling [21].

One of the potential photochemical applications of perylene dyes is the photosensitized singlet-oxygen generation, e.g., within photodynamic therapy [22]. In this process, the photosensitizer, in this case the perylene chromophore, is excited and transfers the absorbed energy to a triplet oxygen $^3O_2$ to generate singlet oxygen $^1O_2$ [23]. As a consequence, the generated $^1O_2$ has a higher reactivity and electrophilicity than $^3O_2$, which makes it more applicable in photochemical and photobiological processes, since the singlet oxygen rapidly reacts with nearby biomolecules leading to destructive reactions, which then causes, for example, the death of cancer cells [24,25]. Such an incorporation of organic chromophores into a rigid framework for photosensitization reactions is already successfully applied for many porphyrin-based metal–organic frameworks [26–28].

Herein, we present the synthesis and characterization of a new 2D zinc coordination-polymer Zn(tpbd)$(DMF)_3$ with the already known perylenediimide (PDI)-based linker molecule 1,6,7,12-tetrachloroperylenediimide-N,N′-di(benzoic acid) (H_2tpdb). Similarly *Hupp* et al. reported a crystalline PDI-zinc framework in 2009, with a different powder pattern, and therefore crystal phase, to the material reported in the present work [29]. Single-crystal X-ray diffraction analysis (SC-XRD) of the materials revealed parallel chromophore packing featuring interchromophoric distances of 3.6 Å, showing a red and blue shifting of the absorption band known indicating as head-to-head aggregation.

Finally, the material was tested in the photosensitization reaction of triplet oxygen to generate singlet oxygen using 1,3-diphenylisobenzofurane as $^1O_2$ trapper, proving that Zn(tpdb)$(DMF)_3$ can be used as an effective material in photochemical reactions. This makes the herein presented material the first example of a PDI-based coordination polymer that is used for photosensitized singlet-oxygen generation.

2. Experimental

2.1. Materials and Method

All utilized chemicals were received from common chemical suppliers and were used without further purification. All air-sensitive reactions were carried out under argon atmosphere (Argon 4.6) using the standard Schlenk techniques. The determination of the elemental composition was performed by the flash combustion method at 1800 °C, onducted by the Microanalytical Lab at the Technical University of Munich. NMR spectra were measured on a Bruker AV400 at ambient temperature at 400 MHz. UV/Vis spectroscopical measurements in solution were performed using a PerkinElmer *Lambda 365*

UV/Vis spectrometer equipped with a xenon lamp. UV/Vis spectroscopical measurements for solid-state samples were performed on a SHIMADZU *UV-3600 Plus* with Ba_2SO_4 as blank. Solution as well as solid-state fluorescence measurements were carried out using an Edinburgh Instruments *FS5* spectrofluorometer equipped with a xenon lamp. BET measurements were performed on a 3Flex Physisorption from Micromeritics Instrument Corp. (Norcross, GA, USA). Single-crystal XRD measurements were conducted in the SC-XRD laboratory of the Catalysis Research Center at the Technical University of Munich (for details cf. Supplementary Materials).

2.2. Synthesis

1,6,7,12-tetrachloro-perylene-3,4,9,10-tetracarboxylic anhydride 1: the synthesis was performed according to a literature-known synthesis [30]. In a 100 mL Schlenk flask, 1 g of perylene-3,4,9,10-tetracarboxylic acid anhydride 1 (2.5 mmol, 1 eq.) and 0.17 g of iodine (0.68 mmol, 0.27 eq.) in 6.55 mL of chlorosulfonic acid were stirred for 2 days at 70 °C under argon atmosphere. After completion, the reaction mixture was slowly poured into 500 mL of ice water. Subsequently, the precipitating orange solid was filtered, washed with water, and dried to produce a bright orange powder (1.32 g, 2.49 mmol, 99%). ^{1}H-NMR (400 mHz, CDCl3): δ (ppm) = 8.75 (s, 4H).

1,6,7,12-tetrachloroperylenediimide-N,N'-di-benzoic acid (H_2tpbd) 2: the synthesis was performed with a modified literature synthesis [31]. In a 100 mL round bottom flask, 1 g of **1** (1.89 mmol, 1 eq.) and 3.88 g of 4-aminobenzoic acid 3 (28.3 mmol, 15 eq.) were dissolved in 25 mL of propionic acid and stirred for 2 days at 160 °C. After the completion of the reaction, the reaction mixture was poured into 100 mL of water and subsequently filtered off. The filtrate is washed with 100 mL of water/methanol (1:1), and afterwards the orange solid was dried to constant weight (1.1 g, 1.89 mmol, 79%).

^{1}H-NMR (400 mHz, DMSO-d6): δ (ppm) = 13.20 (s, 2H, COOH), 8.64 (s, 4H), 8.16–8.12 (m, 4H), 7.61–7.56 (m, 4H).

Zn(tpdb)(DMF)$_3$ 3: in a 4 mL screw-cap vial, $Zn(NO_3)_2$ (15.0 mg, 0.05 mmol, 3.8 eq.) and H_2tpbd **2** (10.0 mg, 0.013 µmol. 1 eq.) were dissolved in 3 mL of DMF. Afterwards, the solution was sonicated and placed for 96 h at 90 °C in an oven. The precipitated solid was then filtered and dried to constant weight to produce orange needles of Zn(tpbd)(DMF)$_3$ **3** (4.13 mg, 0.0039 mmol, 30%).

Elemental analysis (%) calc. for Zn(tpdb)(DMF)$_3$: C, 53.17; H, 3.17; N, 6.66; Zn, 6.22; Cl, 13.49; found C, 53.57; H, 2.78; N, 6.03; Zn, 6.2; Cl, 13.0.

2.3. $^1O_2$ Evolution Experiments

In a glovebox, a 20 mL phototube was filled with 1.25 mg (4.62 mmol, 1 eq.) of DBPF and 1 eq. of the respective photosensitizer **2** or **3**. A total of 5 mL of dried acetonitrile was added with argon counter flow, and subsequently the suspension was stirred for 30 min in the dark to achieve the adsorption/desorption equilibrium under an oxygen atmosphere. Afterwards, an LED with a wavelength of 512 nm was used and at defined time intervals, aliquots of the reaction solution were obtained, diluted, and investigated byUV/Vis-spectroscopy.

3. Results and Discussion

3.1. Linker and CP Synthesis

The PDI-based linker **2** was synthesized in a two-step synthesis procedure starting from perylene-3,4,9,10-tetracarboxylic acid anhydride (Figure 1). In the first step, the bay area positions of the perylene core were chlorinated to twist the aromatic system and later enhance the solubility of the linker for CP synthesis [32]. Subsequently, **1** was reacted with 4-amino benzoic acid to obtain an orange powder of H_2tpbd **2** in good yields of 79% and excellent purity.

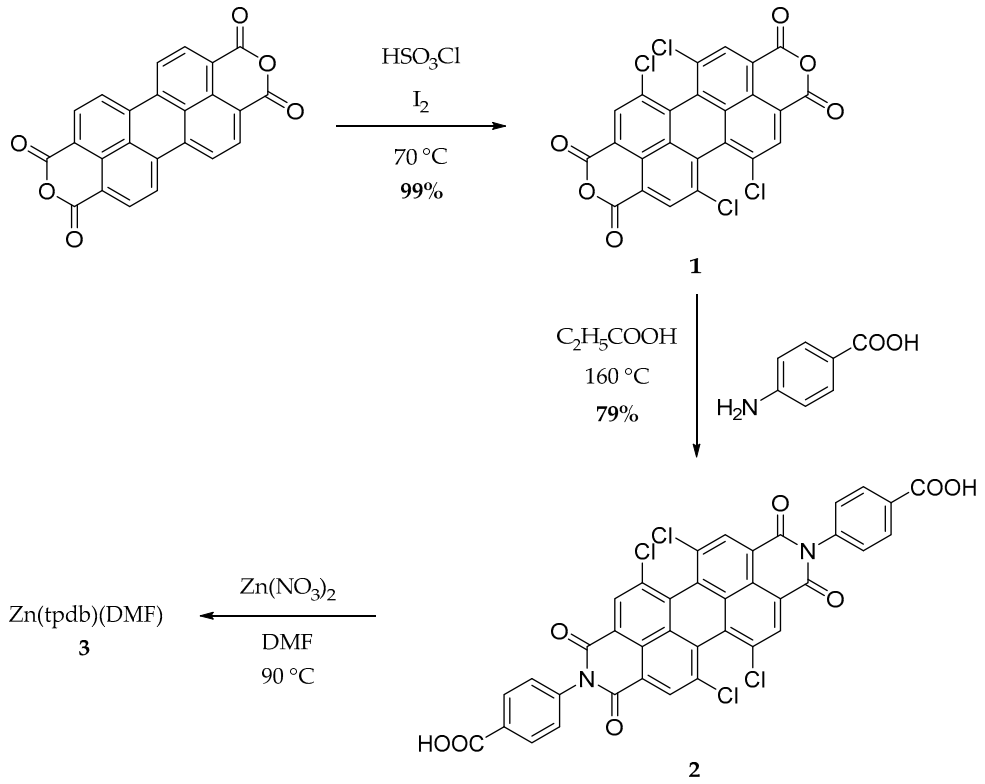

Figure 1. Three-step synthesis procedure to obtain **3**, starting from perylene-3,4,9,10-tetracarboxylic acid anhydride.

Then, 10 mg of **2** were used in a solvothermal synthesis reaction towards novel coordination polymers with 3.8 eq. of $Zn(NO_3)_2$ in 3 mL of DMF for 4 days at 90 °C in an oven. Following this, orange single crystals of $Zn(tpdb)(DMF)_3$ **3** were obtained, which were filtered off and washed with DMF.

In comparison to the other CPs or MOFs, the solvothermal synthesis applied here is comparably uncomplicated (compare Table 1), as it requires no preformation of SBUs or additional additives (e.g., MeOH, trifluoroacetic acid).

Table 1. Table of different literature-known MOF synthesis approaches.

MOF Name	Linker	Metal Salt	Temperature	Solvent	Additives	Refs.
MOF-5, IRMOF(2-20)	R_1-7-BDC, 2,6-NDC, BPDC, HPDC, PDC, TPDC	$Zn(NO_3)_2$	85° to 105 °C	(DMF/DEF), chlorobenzene	H_2O_2, NEt_3	[6,33]
$[Zn_2(TPOM)(NDC)_2]$	TPOM, H_2NDC	$Zn(NO_3)_2$	100 °C	DMF	H_2O	[34]
{[Zn(μ-4-hzba)2]2·4(H2O)}n	4-hydrazinebenzoic acid	$Zn(OAc)_2$	110 °C	EtOH	H_2O	[35]

3.2. Crystal Structure Analysis of H_2tpbd

Small single crystals of H_2tpbd for single-crystal X-ray diffraction (SCXRD) analysis were obtained by controlled crystal growth through the slow diffusion of pentane into a linker solution of 2 (THF). In Figure 2a, the molecular structure, as well as the packing alongside the crystallographic *a* and *c* axis, are depicted (Figure 2b,c).

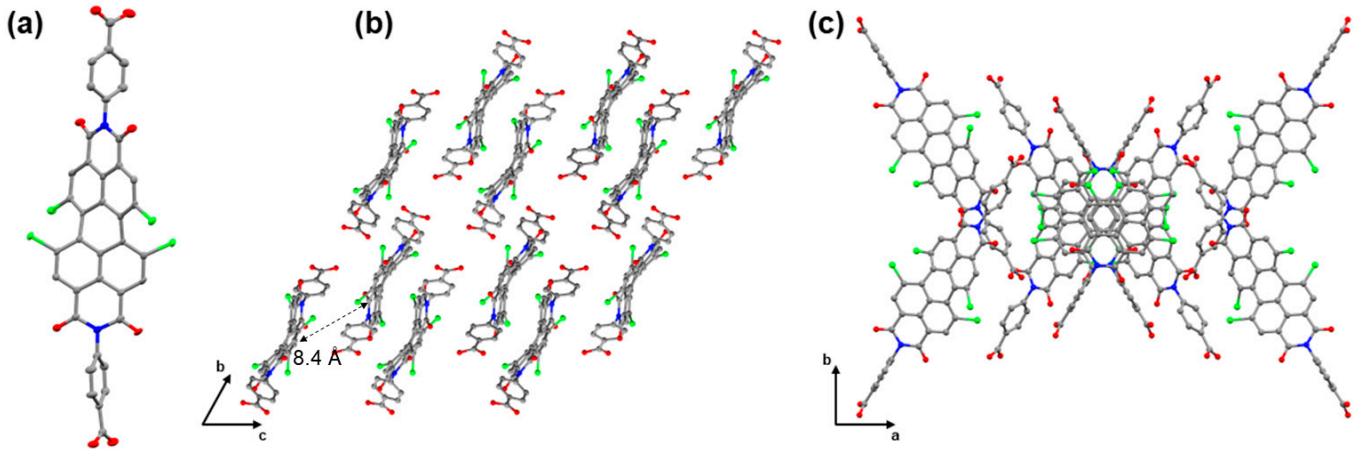

Figure 2. (**a**) ORTEP representation of the molecular structure of the linker molecule H_2tpbd **2** in the solid state, with displacement ellipsoids shown at the 50% probability level. (**b**) Parallel packing of **2** alongside the *b*-*c* plane showing a mean linker distance of 8.4 Å. (**c**) Packing of the **2** alongside the a-b plane showing an alternating arrangement along the *c*-axis. Hydrogen atoms and co-crystallized solvent are omitted for clarity. Color coding: gray = carbon, blue = nitrogen, red = oxygen, and green = chlorine.

The chromophore molecule crystallizes in the monoclinic space group C 2/*c* with unit cell lengths of *a* = 35.229(4) Å, *b* = 12.367(13) Å and *c* = 21.757(3) Å, and monoclinic angle β = 119.954(6)°. The asymmetric unit shows a single molecule of the PDI linker, accompanied by two co-crystallized THF molecules. As expected, the substituted PDI core twists by 35°, compared to the unsubstituted PDI chromophores, caused by the steric demand of the chlorine atoms [32]. This also has an impact on the solubility, since π stacking of the benzene rings is less favored, which makes the molecule more soluble. Interestingly, one of the benzene rings of the benzoic acid group is rotated out of the PDI-imide moiety by roughly 90°, whereas the opposing one shows a respective torsion angle of 78°. The view along the *a*-axis shows the parallel packing of the linker molecules (Figure 2b), with a center-to-center chromophore distance of 8.4 Å. Additionally, in Figure 2c, the alternating packing of the PDI along the a-b plane is depicted.

3.3. Crystal Structure Analysis of Zn(tpbd)(DMF)$_3$

The SC-XRD analysis of the synthesized coordination polymer revealed that the material crystallizes in the monoclinic space group C 2/*c* with unit cell parameters of *a* = 50.894(3) Å, *b* = 19.971(12) Å and *c* = 16.31(10) Å, as well as monoclinic angle β = 91.825(2)°. Two linker molecules and two zinc atoms are present in the asymmetric unit.

In Figure 3a,b the 2D crystalline network is depicted along the *c*-axis and the *b*-axis, showing the linker molecules being arranged as parallel, as well as head-to-tail oriented, to each other. This can also be seen from the topology analysis shown in Figure 3c,d, revealing a four-connecting uninodal net, with an alternating packing that is similar to the linker in the solid state. Additionally, each zinc atom bridges two linkers and additionally coordinates two dimethylformamide molecules, forming a tetrahedral zinc-oxo cluster (Figure 3e). In Figure 3f, the head-to-head chromophore packing of the chromophore is depicted, with a distance of 3.6 Å, and a head-to-tail center of gravity distance of 27.3 Å, which has a great influence on the photophysical behavior of the material.

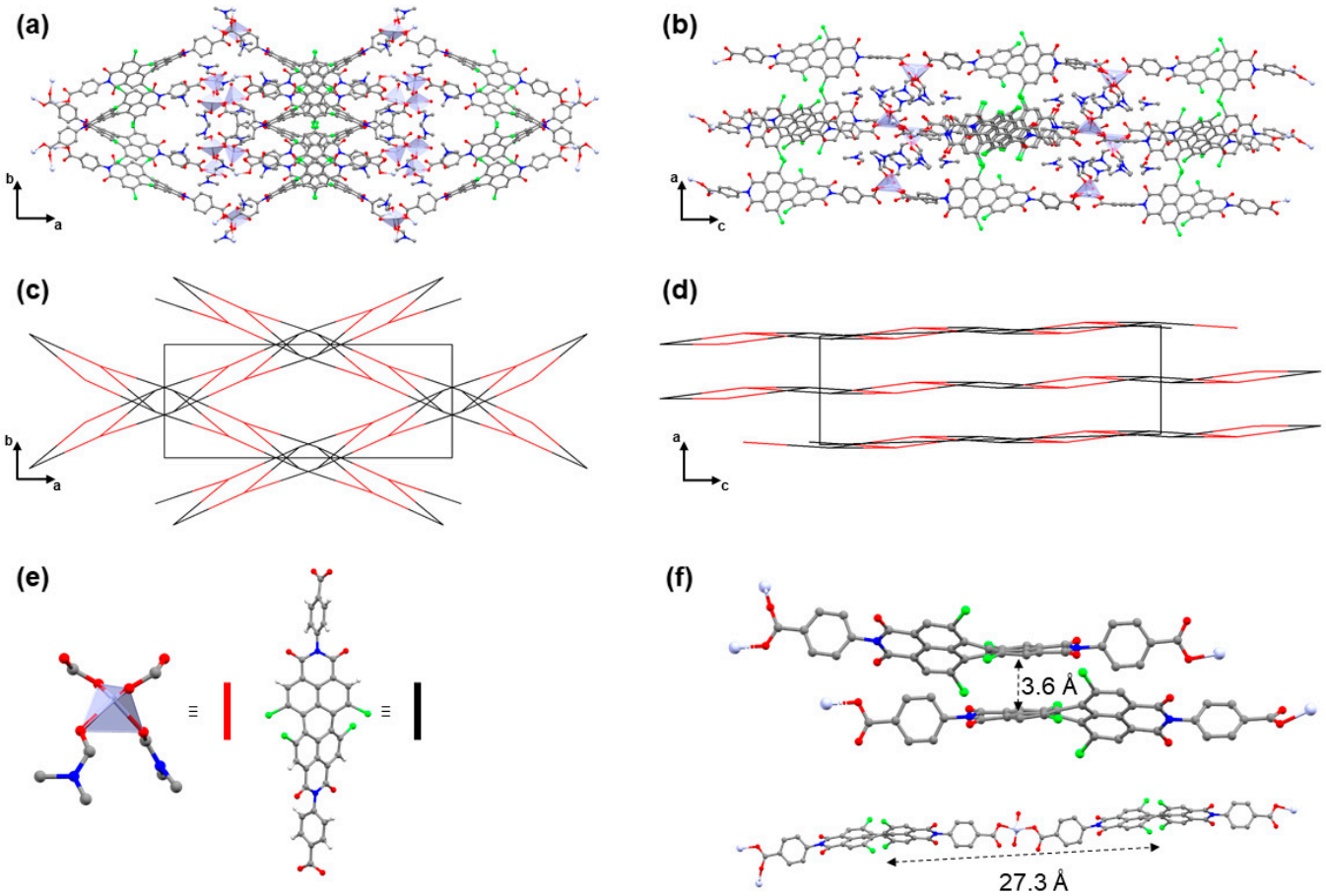

Figure 3. (**a**) Depiction of the crystal structure of the Zn(tpbd)(DMF)$_3$ network along the *c*-axis. (**b**) Parallel packing of chromophore linkers in the 2D framework along the a-c plane. (**c**) Underlying network topology of the 4-c uninodal net alongside the *c*-axis (color coding cf. Figure 3e). (**d**) Depiction of the parallel packing of the underlying network along the *b*-axis (color coding cf. Figure 3e). (**e**) Zn^{2+}-containing tetrahedral SBU (zinc = gray, carbon = dark gray, oxygen = red, and nitrogen = blue), and the representation of the two-connecting linkers. (**f**) Depiction of the head-to-head and head-to-tail arrangement of the linker molecule inside the framework. Hydrogen atoms are omitted for clarity. Color coding: gray = carbon, blue = nitrogen, red = oxygen, green = chlorine, and light gray = zinc.

The powder X-ray diffractogram of the coordination polymer is depicted in Figure 4, which shows high crystallinity and pronounced reflections at 3.59°, 7.01°, and 10.75°, compared to the already-known literature compound presented by *Hupp* et al., showing reflections at 7°, 21°, and 39°. Furthermore, the previously published material showed a high surface area, whereas Zn(tpdb) shows no porosity (cf. Figure S8), proving that the reported material in the present study is a novel framework. Pawley fitting on this data revealed only a small deviation of the fitted curve and measured data, and an R_{wp} of 2.59% and a GoF of 1.92, which supports the determined structure model.

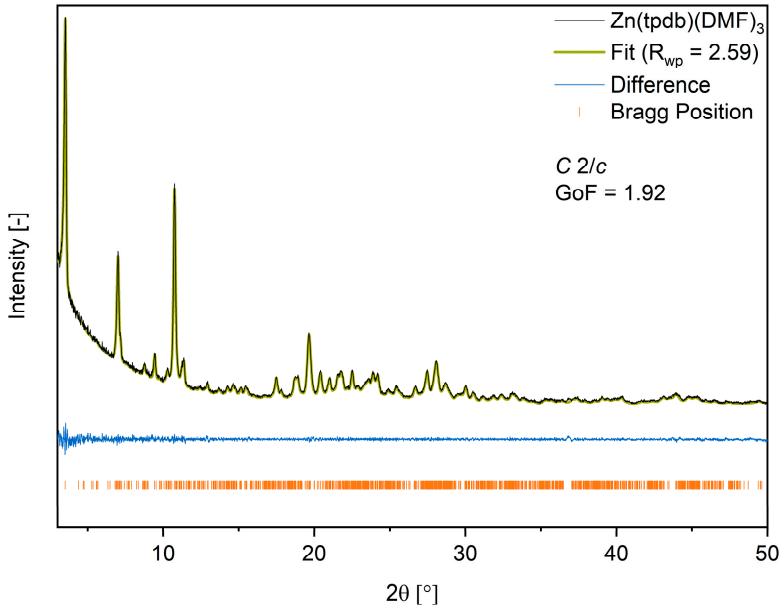

Figure 4. Experimental powder X-ray diffractogram of the Zn(tpdb)-CP (gray), the simulated Pawley fit on the measured data (green), the difference plot (blue), and the Bragg positions (orange).

3.4. Photophysical Characterization of H_2tpdb and Zn(tpdb)(DMF)$_3$

Following the structural investigation of Zn(tpdb)(DMF)$_3$ and H_2tpdb, the photophysical properties of both compounds were examined. The UV/Vis spectrum of **2** shows an absorption band with a maximum absorption at 516 nm, which is comparable to other common perylene chromophores [32]. In contrast, the absorption properties of the CP are different (cf. Figure 5). The respective UV/Vis spectrum shows additional absorption bands with bathochromic and hypochromic shifts. Therefore, the light absorption improved upon the incorporation of the chromophore into the MOF, thus covering a broader spectral range of the electromagnetic spectrum.

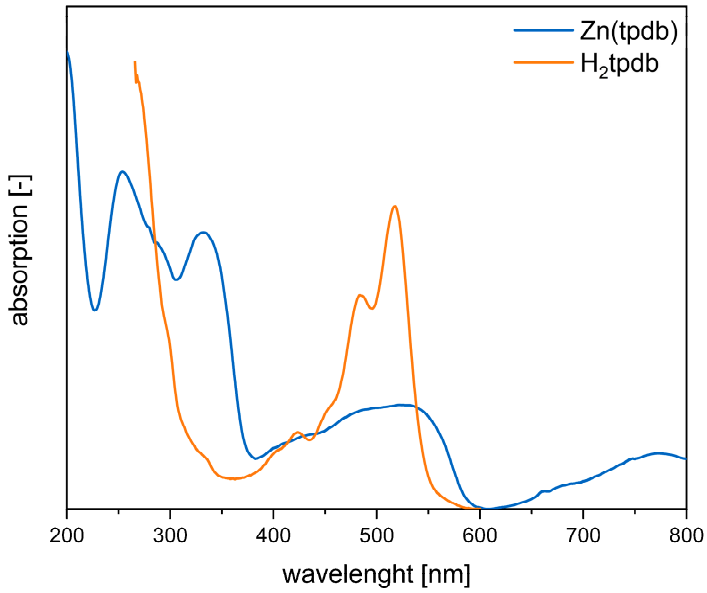

Figure 5. Solid state UV/Vis spectrum of **3** (blue) in comparison to **2** (orange) in the DMF solution. This shows a shift in the spectra of the absorption band of **3**, compared to the absorption band of **2**. Additional to the original absorption band of **2**, **3** shows absorption bands at 760 nm, 260 nm, and 440 nm, which are shifting hypsochromic and bathochromic.

The two mainly discussed aggregation types are the head-to-tail (J-type) and head-to-head (H-type) aggregates (Figure 6) [21].

H-type aggregates promote n-type mobility, which is helpful in electronic devices, while J-type aggregates elevate exciton mobility for optical devices and applications [22]. Furthermore, H-type aggregates are associated with a hypsochromic shift of the bands in the spectrum and J-type aggregates with a bathochromic shift (cf. Figure 6) [23].

Thus, the UV/Vis spectrum of Zn(tpdb)$(DMF)_3$ points towards H-type aggregation behavior, as the absorption band at 516 nm shifts hypsochromic (cf. Figure 5). Furthermore, bathochromic shifting compared to the absorption band of **2** can be observed in the absorption bands of **3**. This shift in the spectrum can be most likely attributed to a charge transfer in the head-to-tail direction of the chromophores (along the crystallographic *c*-axis), since the transition dipole moments of the chromophores are aligned longitudinally to each other (Figure 3f). Additionally, J-type aggregates might be a possible explanation, but are supposed to be unlikely for PDI dyes in extended MOF structures [36,37].

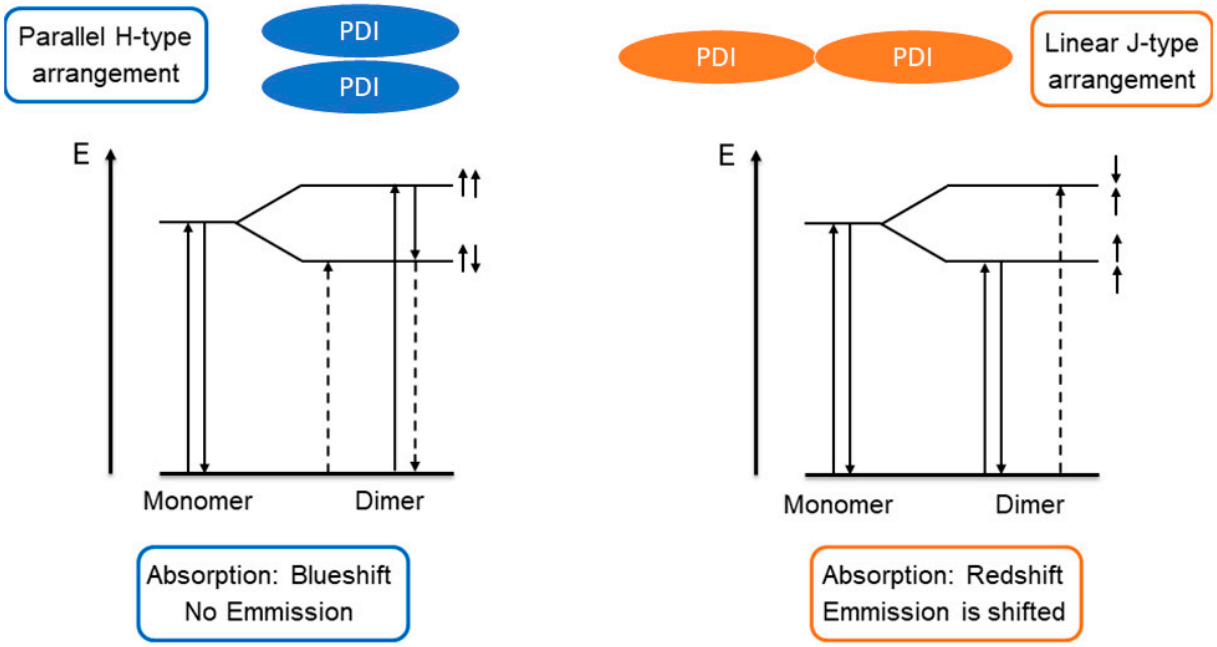

Figure 6. Jablonski diagram of the comparison of the absorption and emission behavior of J- and H-type aggregates [38].

These attributions are supported by an inspection of the emission spectra of **2** and coordination polymer **3** (Figure S4). The CP shows a low-emission intensity when compared to **2**, which can be explained by the high contribution of H-type aggregates, as observed in the UV/Vis spectrum. In general, H-type aggregates quench the emission of the chromophores and promote radiationless energy decay after an internal conversion to the lowest excited state following *Kasha's rule* (Figure 6) [39]. The remaining emission of **3**, despite the presence of H-type aggregates, might be explained by the defects or emission from the surface of the CP, as in both cases, the H-type aggregation might be disturbed.

3.5. Photosensitization Studies

Since we observed the dominant influence of H-type aggregation in **3** within the photophysical studies, the evolution of singlet oxygen under visible light irradiation was tested as the aggregation behavior was shown to be advantageous, compared to unaggregated chromophores in MOFs in the evolution of $^1O_2$ [40]. This reaction has already been reported for different kinds of PDI assemblies, for example, polymers and metal–organic polyhedrons [41,42]. It has also been successfully transferred into MOFs [43], and we present the first example of a PDI linker-based CP within this application.

The activity of the photosensitizer is monitored with 1,3-diphenylisobenzofurane (DBPF), as it is a known $^1O_2$-trapping agent and the reaction can be monitored via UV/Vis spectroscopy following the decrease in the absorption intensity of the aromatic band of DBPF at 416 nm (Figure 7) [44].

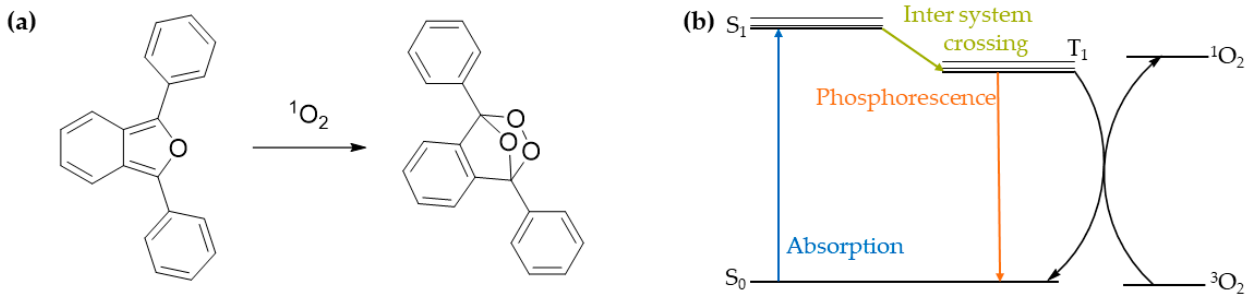

Figure 7. Schematic representation of the photosensitized oxygen activation process applied in this work: (**a**) reaction of $^1O_2$ with 1,3-Diphenylisobenzofuran (DBPF) to obtain the peroxide bridged UV/Vis inactive species. (**b**) Jablonski diagram of the excitation from the $^3O_2$-to-$^1O_2$ trough inter-system crossing enhanced by H-type aggregates adapted from [45].

First, **2** was studied to observe if the chromophore shows any activity. Using a 1:1 molar ratio of linker DBPF in MeCN under argon, an oxygen atmosphere was applied after measuring the first data point, and, subsequently, further data points were recorded after fixed time intervals. Then, **2** was observed to show a high activity towards singlet-oxygen generation, as can be observed in the UV/Vis spectrum (Figure 8a and Figure S5). After six minutes, DBPF is completely consumed by $^1O_2$ generated by the dispersed linker in MeCN. To check if this activity is retained in the coordination polymer, the performance of **3** was tested using the same conditions described for **2**. To our delight, we were able to observe that **3** also successfully generates $^1O_2$ upon light irradiation, as the absorption band of DBPF completely seizes (Figure 8b). We checked that **3** was still stable after the reaction and it remained in a crystalline state (Figure S10). Additionally, control experiments were carried out to test the stability of DBPF under light irradiation and in the presence of **3** without light. These show the stability of DBPF under the chosen conditions (Figure 8a, Figures S7 and S8). In direct comparison, the photosensitization process using **3** is approximately three times slower compared to the **2** (Figure 8a), potentially caused by diffusion limitations within the dispersed CP particles. This is in accordance with previous studies, which also compared the homogenous catalysis of PDI chromophores to a heterogenous catalyst incorporating the same PDIs, showing a decreased $^1O_2$-evolution activity upon incorporation [42]. This is also consistent with several other studies, which show that the use of solid materials decelerates the $^1O_2$ exciation [46]. However, to the best of our knowledge, this is the first example of a PDI-based CP being successfully used as a photosensitizer for singlet-oxygen generation. In general, the incorporation into CPs or MOFs offers key advantages towards future material development, including the modulation of chromophore alignment and material porosity, to specifically address the aggregation and potential diffusion limitations.

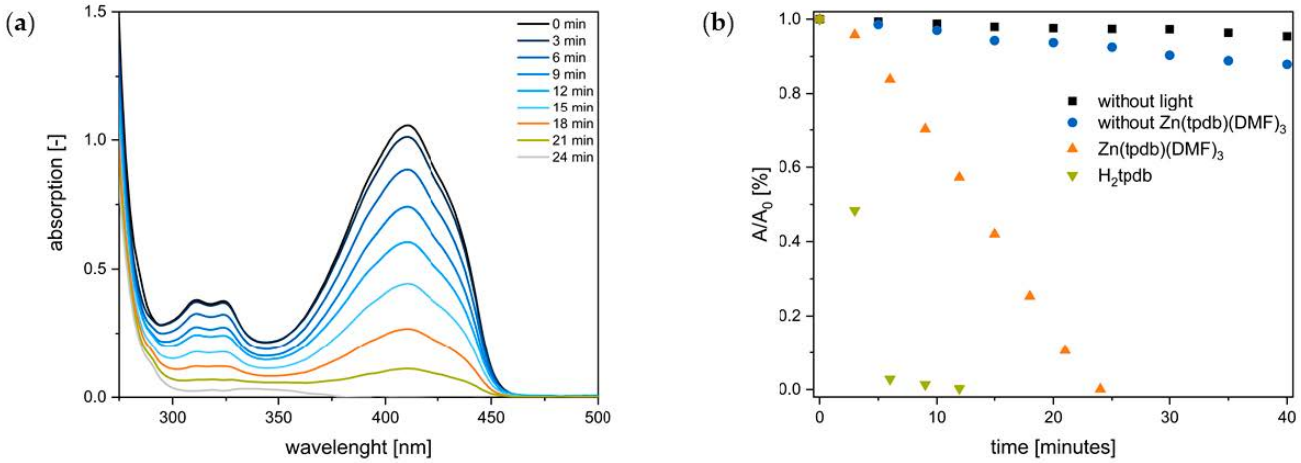

Figure 8. UV/Vis spectroscopic data monitoring the photosensitized $^1O_2$ evolution using linker **2** and CP **3**: (**a**) stacked UV/Vis spectra of 1,3-diphenylisobenzofurane (DBPF) showing the decrease in absorption over time for the reaction with the **3** used as a photosensitizer with a 512 nm LED. (**b**) Decrease in the absorption maxima of DBPF at 416 nm measured from the share of starting absorption at t = 0 min. The decrease in the absorption of DBPF with **3** and linker **2** under light irradiation are presented. In comparison, the control experiments of the DBPF solution with only **3** (black) or only light irradiated (blue) are shown over the duration of 40 min. (**a**) Stacked UV/Vis spectra of DBPF showing the decrease in absorption over time for the reaction with **3** used as a photosensitizer.

4. Conclusions

We synthesized and structurally characterized a new 2D-coordination polymer Zn(tpdb)$(DMF)_3$ **3** based on a PDI-based ditopic linker H_2tpdb **2**. The photophysical properties of the linker and the CP were investigated, revealing a low quantum yield of the luminescence of the CP compared to that of the linker, most likely being caused by H-type aggregation associated with radiationless energy decay within the CP. However, the CP shows desirable absorption properties, since the material covers a broad range of the electromagnetic spectrum desired in mimicking the photosynthesis. Therefore, both the linker and CP were investigated concerning their activity in the photosensitized $^1O_2$ evolution, which is known to be promoted by the aggregation of chromophores. Ultimately, the linker shows activity, which can be retained upon its incorporation into the PDI-based CP, although it is slowed down by a factor of approximately three. Nevertheless, to the best of our knowledge, this is the first example of a PDI-based CP successfully employed for singlet-oxygen generation.

Supplementary Materials: The following supporting information can be downloaded at: https://www.mdpi.com/article/10.3390/en15072437/s1, Figure S1: Thermal gravimetric analysis of Zn(tpdb) from 25 °C to 800 °C with a rate of 10 K min^{-1}. The weight loss of 10% starting at 150 °C indicates the loss of weight the in the structure included water. The subsequent weight loss of 5% starting at 300 °C corresponds to the stored DMF in the structure. The CP structure is then stable until 400 °C. At this temperature, the CP starts to decompose. Figure S2: ^{1}H-NMR of 1,6,7,12-tetrachloro-perylene-3,4,9,10-tetracarboxylic anhydride (1) in $CDCl_3$ showing a single singulett, according to the H atoms in the bay area of the perylene. Figure S3: ^{1}H-NMR of 1,6,7,12-tetrachloroperylenediimide-N,N′-di-benzoic acid (2) in DMSO-d6 showing a singlet at 13.2 ppm for the carboxylic acid groups and an additional singlet at 8.64 ppm for the H atoms in the bay area of the perylene. Additionally, two multipletts can be observed, accounting for the aromatic H atoms of the benzoic acid at 8.15 ppm and 7.59 ppm. Figure S4: Comparison of the emission behavior of 2 and 3. The linker shows a much stronger emission than the CP (compare QY(H_2tpbd) = 0.9 vs. QY(Zn(tpbd)) = < 0.01), suggesting H-type aggregated perylenes, which show a high n-type mobility and quenching of the absorbed light energy, not allowing for directed energy transfer. Figure S5: UV/Vis of the decrease in absorption intensity of DBPF during the reaction with $^1O_2$ produced by linker 2. Figure S6: Control experiment of DBPF

with CP 3 and without light irradiation over the duration of 40 min. Figure S7: Control experiment of DBPF without CP 3 and with light irradiation over the duration of 40 min. Figure S8: BET data of Zn(tpdb)$(DMF)_3$ showing the low surface area of it because of missing pores and the layer structure of the 2D coordination polymer. (a) Semi-log plot of the nitrogen isotherm at 77 K of Zn(tpdb)$(DMF)_3$. (b) BET plot with linear-fit control parameters and calculated monolayer capacity (Q_m). Figure S9: IR data of (a) linker 2 and (b) CP 3. Figure S10: PXRD of the CP after catalysis.

Author Contributions: Conceptualization and writing—original draft preparation, S.N.D., S.J.W., methodology, S.N.D, S.J.W., and A.P., writing—review and editing, A.P. and R.A.F., project administration, R.A.F. All authors have read and agreed to the published version of the manuscript.

Funding: This research was funded by the German Research Foundation (DFG) [EXC 2089] and the Priority Programme COORNETs [SPP 1928].

Acknowledgments: The TUM is greatly acknowledged for institutional funding. S.D. and S.J.W. thank the TUM Graduate School for financial support.

Conflicts of Interest: The authors declare no conflict of interest.

References

1. Barnett, T.P.; Pierce, D.W.; Schnur, R. Detection of Anthropogenic Climate Change in the World's Oceans. *Science* **2001**, *292*, 270–274. [CrossRef] [PubMed]
2. Janna Olmos, J.D.; Kargul, J. A quest for the artificial leaf. *Int. J. Biochem. Cell Biol.* **2015**, *66*, 37–44. [CrossRef] [PubMed]
3. Whittingham, C.P. The chemical mechanism of photosynthesis. *Bot. Rev.* **1952**, *18*, 245–290. [CrossRef]
4. Michl, J. Towards an artificial leaf? *Nat. Chem.* **2011**, *3*, 268–269. [CrossRef]
5. Nocera, D.G. The Artificial Leaf. *Acc. Chem. Res.* **2012**, *45*, 767–776. [CrossRef]
6. Li, H.; Eddaoudi, M.; O'Keeffe, M.; Yaghi, O.M. Design and synthesis of an exceptionally stable and highly porous metalorganic framework. *Nature* **1999**, *402*, 276–279. [CrossRef]
7. Dhakshinamoorthy, A.; Asiri, A.M.; García, H. Metal–Organic Framework (MOF) Compounds: Photocatalysts for Redox Reactions and Solar Fuel Production. *Angew. Chem. Int. Ed.* **2016**, *55*, 5414–5445. [CrossRef]
8. Medishetty, R.; Nemec, L.; Nalla, V.; Henke, S.; Samoć, M.; Reuter, K.; Fischer, R.A. Multi-Photon Absorption in Metal–Organic Frameworks. *Angew. Chem. Int. Ed.* **2017**, *56*, 14743–14748. [CrossRef]
9. Zhu, J.; Shaikh, S.; Mayhall, N.; Morris, A. Energy Transfer in Metal-Organic Frameworks. In *Elaboration and Applications of Metal-Organic Frameworks*; World Scientific: Singapore, 2018; Volume 2, pp. 581–654.
10. Lephalala, M.; Kanchi, S.; Sabela, M.I.; Bisetty, K. Electrochemical Enzymatic Biosensing of Neotame Supported by Computational Methods. *Electroanalysis* **2020**, *32*, 2669–2680. [CrossRef]
11. Sajjadi, S.; Khataee, A.; Bagheri, N.; Kobya, M.; Şenocak, A.; Demirbas, E.; Karaoğlu, A.G. Degradation of diazinon pesticide using catalyzed persulfate with Fe_3O_4@MOF-2 nanocomposite under ultrasound irradiation. *J. Ind. Eng. Chem.* **2019**, *77*, 280–290. [CrossRef]
12. Şenocak, A.; Khataee, A.; Demirbas, E.; Doustkhah, E. Ultrasensitive detection of rutin antioxidant through a magnetic micro-mesoporous graphitized carbon wrapped Co nanoarchitecture. *Sens. Actuators B Chem.* **2020**, *312*, 127939. [CrossRef]
13. Şenocak, A.; Tümay, S.O.; Ömeroğlu, İ.; Şanko, V. Crosslinker polycarbazole supported magnetite MOF@CNT hybrid material for synergetic and selective voltammetric determination of adenine and guanine. *J. Electroanal. Chem.* **2022**, *905*, 115963. [CrossRef]
14. Kent, C.A.; Mehl, B.P.; Ma, L.; Papanikolas, J.M.; Meyer, T.J.; Lin, W. Energy Transfer Dynamics in Metal−Organic Frameworks. *J. Am. Chem. Soc.* **2010**, *132*, 12767–12769. [CrossRef]
15. Würthner, F. Perylene bisimide dyes as versatile building blocks for functional supramolecular architectures. *Chem. Commun.* **2004**, 1564–1579. [CrossRef] [PubMed]
16. Troeger, A.; Ledendecker, M.; Margraf, J.T.; Sgobba, V.; Guldi, D.M.; Vieweg, B.F.; Spiecker, E.; Suraru, S.-L.; Würthner, F. p-Doped Multiwall Carbon Nanotube/Perylene Diimide Derivative Photoelectrochemical Cells for Photocurrent Generation. *Adv. Energy Mater.* **2012**, *2*, 536–540. [CrossRef]
17. Zhao, F.-J.; Zhang, G.; Ju, Z.; Tan, Y.-X.; Yuan, D. The Combination of Charge and Energy Transfer Processes in MOFs for Efficient Photocatalytic Oxidative Coupling of Amines. *Inorg. Chem.* **2020**, *59*, 3297–3303. [CrossRef] [PubMed]
18. Almuhana, A.R.Y.; Langer, P.; Griffin, S.L.; Lodge, R.W.; Rance, G.A.; Champness, N.R. Retention of perylene diimide optical properties in solid-state materials through tethering to nanodiamonds. *J. Mater. Chem. C* **2021**, *9*, 10317–10323. [CrossRef]
19. Haddow, S.L.; Ring, D.J.; Bagha, H.; Pearce, N.; Nowell, H.; Blake, A.J.; Lewis, W.; McMaster, J.; Champness, N.R. Perylene Diimide Triple Helix Formation in the Solid State. *Cryst. Growth Des.* **2018**, *18*, 802–807. [CrossRef]
20. Weissman, H.; Shirman, E.; Ben-Moshe, T.; Cohen, R.; Leitus, G.; Shimon, L.J.W.; Rybtchinski, B. Palladium Complexes of Perylene Diimides: Strong Fluorescence Despite Direct Attachment of Late Transition Metals to Organic Dyes. *Inorg. Chem.* **2007**, *46*, 4790–4792. [CrossRef]

21. Dinçalp, H.; Kızılok, Ş.; İçli, S. Fluorescent macromolecular perylene diimides containing pyrene or indole units in bay positions. *Dye. Pigment.* **2010**, *86*, 32–41. [CrossRef]
22. DeRosa, M.C.; Crutchley, R.J. Photosensitized singlet oxygen and its applications. *Coord. Chem. Rev.* **2002**, *233-234*, 351–371. [CrossRef]
23. Tanaka, F.; Tsumura, K.; Furuta, T.; Iwamoto, K.; Okamoto, M. Efficiencies of singlet oxygen production and rate constants for oxygen quenching in the S1 state of dicyanonaphthalenes and related compounds. *Photochem. Photobiol. Sci.* **2008**, *7*, 56–62. [CrossRef] [PubMed]
24. Pibiri, I.; Buscemi, S.; Palumbo Piccionello, A.; Pace, A. Photochemically Produced Singlet Oxygen: Applications and Perspectives. *ChemPhotoChem* **2018**, *2*, 535–547. [CrossRef]
25. Chen, J.; Keltner, L.; Christophersen, J.; Zheng, F.; Krouse, M.; Singhal, A.; Wang, S.-s. New Technology for Deep Light Distribution in Tissue for Phototherapy. *Cancer J.* **2002**, 8. [CrossRef] [PubMed]
26. Wang, J.; Zhang, X.; Liu, Y.; Wang, Z.; Wang, P.; Zheng, Z.; Cheng, H.; Dai, Y.; Huang, B. Enhanced singlet oxygen production over a photocatalytic stable metal organic framework composed of porphyrin and Ag. *J. Colloid Interface Sci.* **2021**, *602*, 300–306. [CrossRef]
27. Ling, P.; Cheng, S.; Chen, N.; Gao, F. Singlet-oxygen generated by a metal–organic framework for electrochemical biosensing. *J. Mater. Chem. B* **2021**, *9*, 4670–4677. [CrossRef] [PubMed]
28. Park, J.; Jiang, Q.; Feng, D.; Zhou, H.-C. Controlled Generation of Singlet Oxygen in Living Cells with Tunable Ratios of the Photochromic Switch in Metal–Organic Frameworks. *Angew. Chem. Int. Ed.* **2016**, *55*, 7188–7193. [CrossRef]
29. Nelson, A.P.; Farha, O.K.; Mulfort, K.L.; Hupp, J.T. Supercritical Processing as a Route to High Internal Surface Areas and Permanent Microporosity in Metal−Organic Framework Materials. *J. Am. Chem. Soc.* **2009**, *131*, 458–460. [CrossRef]
30. Yoshinaga, K.; Swager, T.M. Fluorofluorescent perylene bisimides. *Synlett* **2018**, *29*, 2509–2514.
31. Addicott, C.; Oesterling, I.; Yamamoto, T.; Müllen, K.; Stang, P.J. Synthesis of a Bis(pyridyl)-Substituted Perylene Diimide Ligand and Incorporation into a Supramolecular Rhomboid and Rectangle via Coordination Driven Self-Assembly. *J. Org. Chem.* **2005**, *70*, 797–801. [CrossRef]
32. Würthner, F.; Saha-Möller, C.R.; Fimmel, B.; Ogi, S.; Leowanawat, P.; Schmidt, D. Perylene Bisimide Dye Assemblies as Archetype Functional Supramolecular Materials. *Chem. Rev.* **2016**, *116*, 962–1052. [CrossRef]
33. Eddaoudi, M.; Kim, J.; Rosi, N.; Vodak, D.; Wachter, J.; O'Keeffe, M.; Yaghi, O.M. Systematic Design of Pore Size and Functionality in Isoreticular MOFs and Their Application in Methane Storage. *Science* **2002**, *295*, 469–472. [CrossRef]
34. Lv, R.; Li, H.; Su, J.; Fu, X.; Yang, B.; Gu, W.; Liu, X. Zinc Metal–Organic Framework for Selective Detection and Differentiation of Fe(III) and Cr(VI) Ions in Aqueous Solution. *Inorg. Chem.* **2017**, *56*, 12348–12356. [CrossRef] [PubMed]
35. Basu, U.; Otto, S.; Heinze, K.; Gasser, G. Biological Evaluation of the NIR-Emissive Ruby Analogue [Cr(ddpd)2][BF4]3 as a Photodynamic Therapy Photosensitizer. *Eur. J. Inorg. Chem.* **2019**, *2019*, 37–41. [CrossRef]
36. Eder, T.; Stangl, T.; Gmelch, M.; Remmerssen, K.; Laux, D.; Höger, S.; Lupton, J.M.; Vogelsang, J. Switching between H- and J-type electronic coupling in single conjugated polymer aggregates. *Nat. Commun.* **2017**, *8*, 1641. [CrossRef] [PubMed]
37. McCarthy, B.D.; Hontz, E.R.; Yost, S.R.; Van Voorhis, T.; Dincă, M. Charge Transfer or J-Coupling? Assignment of an Unexpected Red-Shifted Absorption Band in a Naphthalenediimide-Based Metal–Organic Framework. *J. Phys. Chem. Lett.* **2013**, *4*, 453–458. [CrossRef]
38. Herbst, S.; Soberats, B.; Leowanawat, P.; Stolte, M.; Lehmann, M.; Würthner, F. Self-assembly of multi-stranded perylene dye J-aggregates in columnar liquid-crystalline phases. *Nat. Commun.* **2018**, *9*, 2646. [CrossRef]
39. Gierschner, J.; Lüer, L.; Milián-Medina, B.; Oelkrug, D.; Egelhaaf, H.-J. Highly Emissive H-Aggregates or Aggregation-Induced Emission Quenching? The Photophysics of All-Trans para-Distyrylbenzene. *J. Phys. Chem. Lett.* **2013**, *4*, 2686–2697. [CrossRef]
40. Feng, X.; Wang, X.; Wang, H.; Wu, H.; Liu, Z.; Zhou, W.; Lin, Q.; Jiang, J. Elucidating J-Aggregation Effect in Boosting Singlet-Oxygen Evolution Using Zirconium–Porphyrin Frameworks: A Comprehensive Structural, Catalytic, and Spectroscopic Study. *ACS Appl. Mater. Interfaces* **2019**, *11*, 45118–45125. [CrossRef]
41. He, L.; Cai, L.-X.; Li, M.-H.; Zhang, G.-L.; Zhou, L.-P.; Chen, T.; Lin, M.-J.; Sun, Q.-F. Designing a highly stable coordination-driven metallacycle for imaging-guided photodynamic cancer theranostics. *Chem. Sci.* **2020**, *11*, 7940–7949. [CrossRef]
42. Blacha-Grzechnik, A.; Drewniak, A.; Walczak, K.Z.; Szindler, M.; Ledwon, P. Efficient generation of singlet oxygen by perylene diimide photosensitizers covalently bound to conjugate polymers. *J. Photochem. Photobiol. A Chem.* **2020**, *388*, 112161. [CrossRef]
43. Meng, A.-N.; Chaihu, L.-X.; Chen, H.-H.; Gu, Z.-Y. Ultrahigh adsorption and singlet-oxygen mediated degradation for efficient synergetic removal of bisphenol A by a stable zirconium-porphyrin metal-organic framework. *Sci. Rep.* **2017**, *7*, 6297. [CrossRef] [PubMed]
44. Rossi, L.M.; Silva, P.R.; Vono, L.L.R.; Fernandes, A.U.; Tada, D.B.; Baptista, M.S. Protoporphyrin IX Nanoparticle Carrier: Preparation, Optical Properties, and Singlet Oxygen Generation. *Langmuir* **2008**, *24*, 12534–12538. [CrossRef] [PubMed]
45. Hynek, J.; Chahal, M.K.; Payne, D.T.; Labuta, J.; Hill, J.P. Porous framework materials for singlet oxygen generation. *Coord. Chem. Rev.* **2020**, *425*, 213541. [CrossRef]
46. Wahlen, J.; De Vos, D.E.; Jacobs, P.A.; Alsters, P.L. Solid Materials as Sources for Synthetically Useful Singlet Oxygen. *Adv. Synth. Catal.* **2004**, *346*, 152–164. [CrossRef]